Dielectric size optimization for high power density in large-scale triboelectric nanogenerators

Abdulkerim Karabiber[1] (✉), Ömer Dirik[1], Feyyaz Koc[1], and Faruk Ozel[2]

[1] *Department of Electrical and Electronics Engineering, Bingol University, Bingol 12000, Turkey*
[2] *Department of Metallurgical and Materials Engineering, Karamanoglu Mehmetbey University, Karaman 70200, Turkey*

ABSTRACT

Triboelectric nanogenerators (TENGs) have emerged as a promising technology to harvest electrical energy from natural motions such as human movement, wind, and water flow. Although TENGs show significant potential in small-scale applications, developing large-scale TENGs capable of generating high power remains a significant challenge. Several factors that can affect the performance of large-scale TENGs are being investigated to overcome this challenge, including the size and configuration of dielectric materials. This study optimizes dielectrics regarding surface area, thickness, and multicell configuration to improve harvested electrical power density in large-scale TENGs. In the studies, glass fiber was used as the positive dielectric, and multi-purpose white silicone was used as the negative dielectric because of their high tribo-potential, durability, and easy accessibility. In the size optimization phase, dielectric thicknesses and surface areas that provide the maximum power density were determined. Subsequently, horizontal and vertical multicell configurations were examined to efficiently integrate size-optimized dielectrics. The results reveal that large-scale TENGs with vertical multicell configurations can achieve high and usable energy density for electronics. The findings provide valuable insight into the development of large-scale TENGs with advanced power generation capabilities.

KEYWORDS

triboelectric nanogenerator, dielectric layer, size optimization, multi-cell structure, high power density

1   Introduction

Triboelectric nanogenerators (TENGs) represent a significant advance as an innovative energy source, especially in self-powered systems, wearable electronics, and sustainable energy solutions. TENGs can generate electricity from small natural movements, such as human motions [1–3], footsteps [4, 5], wind [6–8], and water waves [9–11]. TENGs can potentially power various electronic devices, including wearable devices [12, 13], sensors [13, 14], and energy storage systems [15, 16]. This technology provides an opportunity to generate energy in daily life by converting wasted or unused mechanical energy into usable electricity. Although TENGs show promising performance as a renewable energy source, their integration into self-powered devices faces several technical and practical obstacles. Solving these challenges is crucial to making TENGs a practical and effective energy source for use in future electronics.

Various strategies can be employed to enhance the power output of TENGs. The first of these strategies is carefully selecting materials that exhibit a high triboelectric effect [17–19]. Incorporating dielectric layers with opposite tribo-potential can amplify TENG power output. Secondly, surface modification techniques, including chemical treatments and nanoscale patterning, can be implemented to improve the contact area between dielectric materials. The improved contact area increases the triboelectric charge density and subsequently enhances power output [20–23]. Thirdly, optimizing the structural design of the

TENG proves instrumental in maximizing the contact area between materials. Different geometries, as well as multi-layered or hierarchical structures, can be explored to enhance the effective surface area [24–26]. Environmental factors, such as temperature, humidity, and pressure, have a significant impact on TENG output performance [27, 28]. Therefore, sensitive control of these parameters is necessary for optimizing TENG performance. Finally, the electrical circuit connected to the TENG can be fine-tuned to increase power output [29–31]. Employing a resonant circuit or a high impedance that matches the TENG output frequency has been demonstrated to be effective in amplifying the power output of TENGs. Collectively, these strategic interventions contribute to a substantial improvement in the power output of TENGs, making them more efficient and reliable for practical applications.

Optimization of dielectric layer thickness and surface area critically affects the energy efficiency of TENGs depending on the tribo-material content and contact-separation structure. Dielectric layer thickness plays a very important role in TENG performance, affecting various parameters. A thinner dielectric layer can increase the electric field strength between the electrostatic layers, leading to a higher output voltage [32–34]. However, this can also increase the risk of electrical failure, reducing the reliability and durability of the device. Conversely, a thicker dielectric layer may reduce the electric field strength and lower the output voltage due to the increased distance between the electrostatic layers. The effective area of the dielectric layers is another important factor

Address correspondence to akarabiber@bingol.edu.tr

affecting TENG performance. A larger effective dielectric area facilitates charge transfer between triboelectric layers, generally resulting in higher output voltages and currents [35, 36]. This increased charge can create a stronger electric field, leading to a higher output voltage. However, expanding the effective area of the dielectric layer may cause higher dielectric losses and parasitic capacitances, potentially reducing the output voltage of the TENGs [37–39].

TENG devices can be integrated to enhance output energy and power small electronic devices. In some experiments, a linear increase in total electrical output was observed with the addition of parallel connected TENG units in up to seventy layers [40]. In another study, corona loading was used to fabricate multilayer TENGs with a focus on optimizing their performance. Among TENGs with up to three layers, the three-layer TENG has been identified as the most efficient, exhibiting the highest electrical charge density [41]. Another notable contribution is the development of a TENG-based self-charging power system for wearable electronics. TENG's multilayer elastomeric structure, characterized by closely stacked arches, not only ensured high efficiency but also robustness, dust resistance, and water resistance when fully enclosed [42]. Additionally, a TENG array consisting of spherical units with a spring-supported multilayer structure is designed to harvest water wave energy. The multilayer design increases space utilization and provides higher efficiency for each spherical unit [43]. Finally, a zigzag-shaped, flexible, and cost-effective five-layer TENG was introduced. This innovative structure has proven to be effective in increasing the electrical output without increasing the overall area of the TENG by providing a compact and lightweight solution [44].

This study initially aimed to determine the optimal dielectric sizes that would provide maximum energy density in contact separation mode TENGs. Research then turned to horizontal and vertical multicell configurations to explore the highly efficient integration of dielectrics fabricated at these optimum sizes. White silicone and glass fiber were chosen as negative and positive dielectrics, respectively, due to their high tribo potential and long mechanical life. In determining the optimum dielectric sizes, the dielectric thicknesses that provide the highest output power density were determined. The most effective surface areas for these optimized thicknesses were then selected. To discover the most effective integration model for TENG layers, both horizontal and vertical multicell TENGs were fabricated using size-optimized dielectrics. The energy produced by the multicell TENGs was compared for different capacitive loads and light-emitting device (LED) applications. The findings indicate that smaller-sized multicell dielectrics generate more energy for a given contact area than single-cell dielectrics with larger sizes. Furthermore, multicell TENGs with vertical multicell designs exhibit greater power efficiency than those with horizontal multicell configurations. These findings are essential for designing and optimizing large-scale TENGs, which have enormous potential for energy harvesting applications.

2 Methods

2.1 Fabrication of TENGs

Figure 1(a) shows the power generation processes of a vertical contact separation mode TENG. In the pressed stage, charges of opposite polarities accumulate on the surfaces of two different dielectric layers, depending on their tendency to donate electrons. During the separation of dielectrics, the balance between the stored charges is disrupted and these charges cause electron transfer between the electrode layers under the influence of the electrostatic field. In the pressed and released stages, charge balance is maintained and there is no flow of electrons. Conversely, in the pressing and releasing stages, the change in charge balance causes an electric current to occur between the electrodes. Figure 1(b) shows the details of the structural model of the TENG. The support layer ensures that the external force applied to the TENG does not damage the dielectrics and is evenly distributed over the surface. The springs placed at the four corners of the TENG create the pushback force during the separation phase. Electrodes glued to the support layer and embedded cables are in electrical contact with each other. Figure S1 in the Electronic Supplementary Material (ESM) shows the circuit connection diagram of the TENGs designed for this study. Two different dielectrics with positive and negative tribo-potential were bonded to the electrodes. Figures 1(c)–1(e) show the spring-assisted
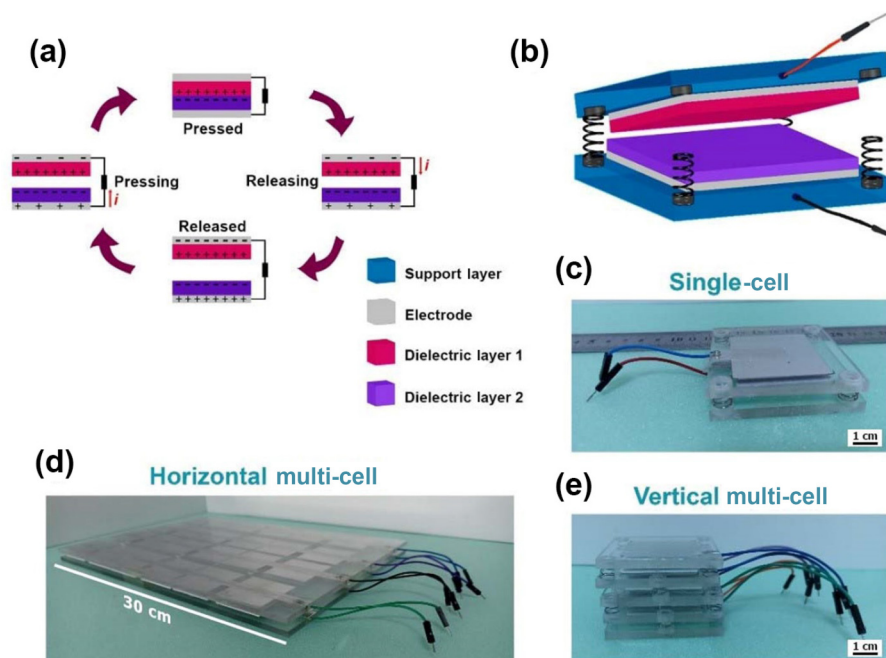

Figure 1 (a) Working stages of a vertical contact separation mode TENG. (b) Spring-assisted TENG design. (c) Single-cell TENG, (d) horizontal multi-cell TENG, and (d) vertical multi-cell TENG.

vertical contact mode TENGs produced for the experiments. In all TENGs, a 0.5 cm thick layer of acrylic is used as the substrate, while the conductive layer is composed of aluminum foil. Each dielectric cell utilized in the TENGs has an area of 4 cm × 4 cm. The negative dielectric material is made of multi-purpose silicone sealant, whereas the positive dielectric material is made of glass fiber with a weight of 100 g/m². Figure 1(c) shows a side view of a 6 cm × 6 cm single-cell TENG with small 0.8 cm diameter springs at four corners. Figure 1(d) shows a side view of a 20 cm × 30 cm horizontal multicell TENG consisting of four subgroups of six cells each. Cells in each subgroup are connected using Al foil and finally soldered to copper wire. Figure 1(e) demonstrates a side view of a vertical multicell TENG, which has dielectrics bonded to both sides of the middle substrates. The springs are positioned at midpoints of the substrate edges, skipping a row, resulting in non-overlapping grooves between the top and bottom springs.

2.2 Measurement and characterization

A specially designed press machine was used as a mechanical pulse generator to measure the tribo-potential of dielectrics of different sizes and thicknesses. The pulse frequency is regulated using a programmable logic circuit (PLC) controller, and the Zemic L6E3 load cell is utilized to measure the pulse force precisely. To measure the voltage produced by TENGs, a Rigol MSO5104 oscilloscope was utilized. The following formulas determined current, power, energy, and total transfer charge. The current generated by the TENGs was calculated using the equation

$$I_{\text{TENG}} = \frac{V_{\text{m}}}{R_{\text{eq}}} \qquad (1)$$

where V_{m} is the measured voltage and R_{eq} is the equivalent resistance between the oscilloscope probes. The calculations were conducted considering the resistance of the oscilloscope, which is 10 MΩ. The power produced by the TENGs was determined using the equation

$$P = I_{\text{TENG}}^2 R_{\text{eq}} \qquad (2)$$

The total transfer charge (Q_{SC}) at the capacitive load was obtained using the equation

$$Q_{\text{SC}} = C_{\text{L}} V_{\text{m}} \qquad (3)$$

where C_{L} is the value of the capacitive load. The energy stored in C_{L} is found with the formula below

$$E_{\text{s}} = \frac{1}{2} C_{\text{L}} V_{\text{m}}^2 \qquad (4)$$

Furthermore, a GW Instek 6200 LCR meter was used to measure the I–V characteristic and capacitance values of the TENGs. The results from the LCR meter were used to identify the permittivity properties of dielectrics. The permittivity (ε^*) can be decomposed into a real part (ε') and an imaginary part (ε''), as described by the following equations

$$\varepsilon^* = \varepsilon' - \mathrm{i}\varepsilon'' \qquad (5)$$

$$\varepsilon' = \frac{C_{\text{m}}}{C_0} \qquad (6)$$

$$\varepsilon'' = \frac{G_{\text{m}}}{\omega C_0} \qquad (7)$$

Here, ε' represents the ability of the material to store electrical energy, and ε'' represents the ability of the material to lose electrical energy as heat. C_{m}, C_0, G_{m}, and ω correspond to the measured capacitance, vacuum capacitance, the measured conductivity, and angular frequency, respectively.

$$C_0 = \frac{\varepsilon_0 A}{d} \qquad (8)$$

$$\omega = 2\pi f \qquad (9)$$

Additionally, A and d represent the area and thickness of the dielectric, while ε_0 denotes the free space permittivity.

3 Results and discussion

3.1 Optimization of dielectric thickness

The triboelectric effect, characterized by the transfer of electrons between materials upon contact, forms the basis of TENGs, promising devices for energy harvesting. Optimizing the dimensions of tribo-materials is crucial for enhancing TENG efficiency. Recent studies have shown that glass fiber and silicon are dielectrics with high tribo potential, easy access, and high impact strength [20, 34, 45]. Rubber-silicone, which solidifies when in contact with air, is a good negative tribo-material that can be easily molded into different designs and its surface morphology can be easily improved. Fiberglass is flexible and has a large surface area due to its fibrous structure; therefore, it has a higher positive tribo potential than solid glass. This study focuses on investigating the optimal dimensions of silicon and glass fiber, key components in vertical contact mode TENGs, to maximize power output. Figure 2(a) displays the output voltages obtained from 4 cm × 4 cm TENGs produced from glass fibers of three different thicknesses (25, 100, and 201 g/m²). The thicknesses of thin, medium and thick glass fibers are 0.030, 0.075, and 0.150 mm, respectively. The thickness of the glass fibers was selected from standard thicknesses that are frequently found on the market and show the highest tribo-potential. The mechanical pulse frequency was set to 2 Hz, and the pulse force was 20 N for the measurements in a short circuit condition. The respective output voltages measured were 87.7, 141.0, and 121.0 V for TENGs produced from thin, medium, and thick glass fiber, respectively. It is observed that the TENG produced from the medium-thick glass fiber produces the highest output voltage, while the thick glass fiber outperforms the thin one. The output voltage of the TENG produced from the medium-thick glass fiber is 66.6% and 16.5% better than the thin and thick ones, respectively. One of the critical factors determining the output power of TENGs is the load characteristic. Depending on the amplitude and angle of the load impedance, the maximum value of the power generated by TENGs may vary. Figure 2(b) shows the output voltages of the TENGs at a pulse frequency of 4 Hz and under a capacitive load of 22 nF. The maximum voltages of the capacitive load were measured as 4.06, 4.63, and 4.40 V, respectively. The output voltage of the TENG produced from the medium glass fiber under capacitive load is 14.0% and 5.2% higher than the thin and thick ones, respectively. The TENG, made of medium glass fiber, works best under capacitive and ohmic loads. However, the increase in output voltage under capacitive load is less than that of ohmic load. There is a nonlinear relationship between the characteristic parameters of dielectrics and the output voltage of the TENGs (Fig. S2 in the ESM) [21, 46]. Glass fibers of different thicknesses cause variations in the equivalent resistance and capacitance of TENGs. These variations affect the output voltage at different rates depending on the impedance value of the load. Consequently, the rate of change in output power observed in ohmic and capacitive loads may differ in TENG devices using various dielectrics.
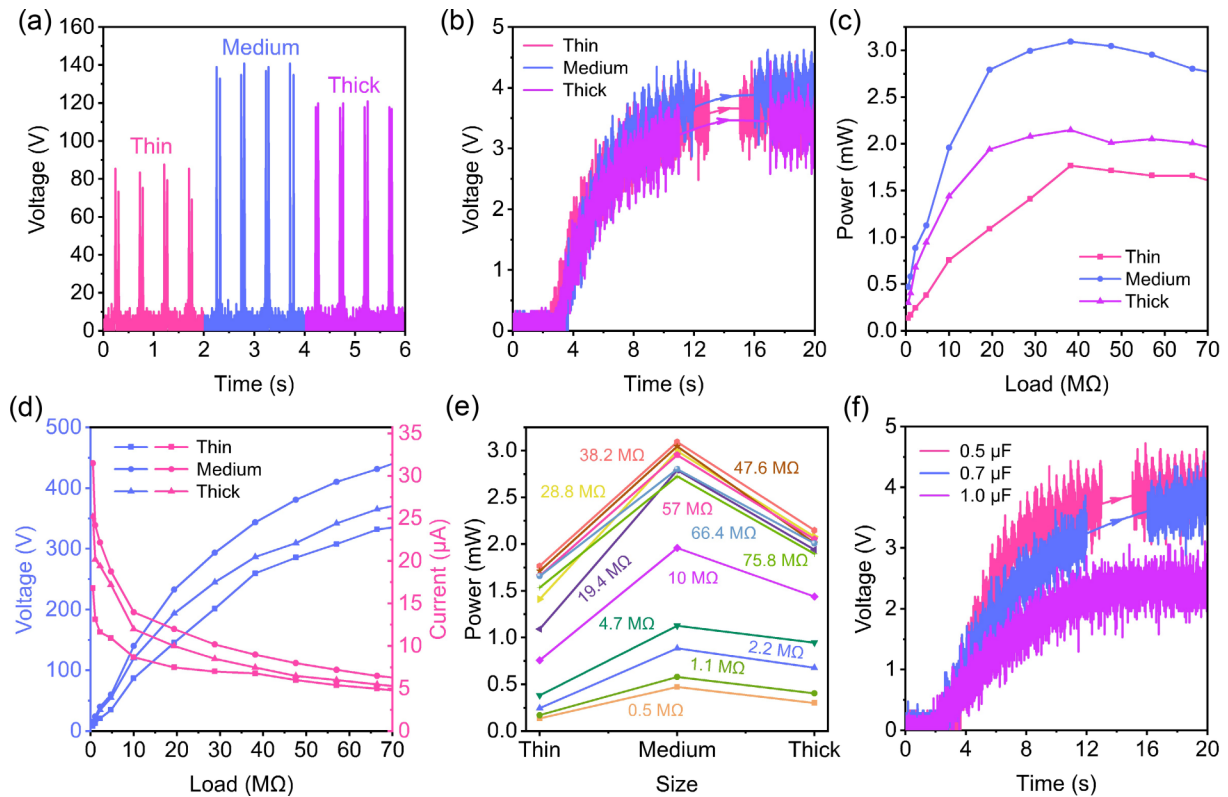
Figure 2 (a) Output voltage of the TENGs produced from glass fibers with different thicknesses. (b) Capacitive load voltage under 4 Hz mechanical pulse. (c) Maximum power under variable load. (d) Current–voltage characteristics of TENGs. (e) Maximum power under variable load. (f) Output voltages of the TENGs produced from medium-thickness glass fiber.

The maximum power produced by TENGs varies depending on the load characteristic. Figure 2(c) illustrates the maximum power curves produced by TENGs at a pulse frequency of 2 Hz and for different ohmic loads. The maximum powers produced by TENGs under an equivalent resistance of 38.2 MΩ are 1.77 mW (1.1 W/m²), 3.10 mW (1.94 W/m²), and 2.15 mW (1.34 W/m²) for the thin, medium, and thick glass fibers, respectively. The TENG with medium thickness provides the highest output power at all loads. Figure 2(d) displays the maximum output voltages and current values obtained from TENGs at different ohmic loads. The maximum output voltages of thin, medium, and thick glass fibers obtained with a 66.4 MΩ resistor are 332.0, 431.6, and 365.2 V, respectively. The maximum current values obtained with a 0.5 MΩ resistor are 16.8, 31.5, and 25.2 μA for the thin, medium, and thick glass fibers, respectively. Figure 2(e) shows the maximum power values obtained at different ohmic loads. The maximum power values obtained from all three TENGs are observed at the 38.2 MΩ resistive load, which are 1.77, 3.10, and 2.15 mW, respectively. Figure 2(f) presents the output voltages obtained under different capacitive loads from TENGs produced from medium-thickness glass fiber. The maximum output voltage values obtained under 0.5, 0.7, and 1.0 μF capacitive loads are 4.59, 4.44, and 3.11 V, respectively.

The thickness of the dielectric material is a crucial factor that affects the amount of energy stored in capacitors. The following equations express the relationship between the dielectric thickness and the electrostatic effect.

$$E = \frac{V}{d} \qquad (10)$$

where E is the electric field strength, V is the applied voltage, and d is the dielectric thickness. Increasing the dielectric thickness in capacitors reduces the electrostatic effect between the capacitor plates, consequently decreasing the energy stored in the capacitor. However, the amount of electric charge on the dielectric is the primary factor influencing the amount of charge transferred. Suppose the dielectric thickness is reduced too much to enhance the electrostatic effect. In that case, it will decrease the charge potential of the dielectrics and subsequently reduce the output voltage of the TENGs. Especially very thin dielectrics with a fibrous structure such as glass fibers cause increased leakage currents and decreased performance of TENGs. Therefore, optimizing the thickness of the dielectrics becomes crucial to maximizing the energy density of TENGs [32, 47].

3.2 Optimization of surface area

Figure 3 presents the measurement results of TENGs with different sizes at various pulse frequencies. Figure 3(a) shows the output voltages of TENGs with five different sizes (4, 9, 16, 25, and 36 cm²) under the mechanical pulse with 100 N force and 2 Hz frequency. The measured voltages are 68, 107, 170, 262, and 282 V, respectively. The maximum voltages increase with the size of the TENGs. Figure 3(b) displays the corresponding maximum current values generated by the TENGs, which are 6.8, 10.7, 17, 26.2, and 28.2 μA, respectively. The current values also rise as the size of the TENGs increases. As shown in Fig. 3(c), the electrical powers produced are 0.46, 1.14, 2.89, 6.86, and 7.95 mW, respectively. The power increase in large TENGs is proportional to the increase in current and voltage. Figure 3(d) shows the output voltages of TENGs under 100 N force and different pulse frequencies of 1, 2, and 3 Hz, which are measured as 40.1, 97.2, 122, 146, and 156 V for 1 Hz, 68, 107, 170, 362, and 282 V for 2 Hz, and 97.2, 122, 214, 297, and 331 V for 3 Hz, respectively. The frequency increase linearly improves the output voltage of TENG. Figure 3(e) shows the corresponding current values generated by the TENGs at three different frequencies, which change similarly to the voltage. Finally, Fig. 3(f) presents the frequency power relationship, where the electrical powers generated by the TENGs are 0.16, 0.94, 1.49, 2.13, and 2.43 mW for 1 Hz, 0.46, 1.14, 2.89, 6.86, and 7.95 mW for 2 Hz, and 0.94,
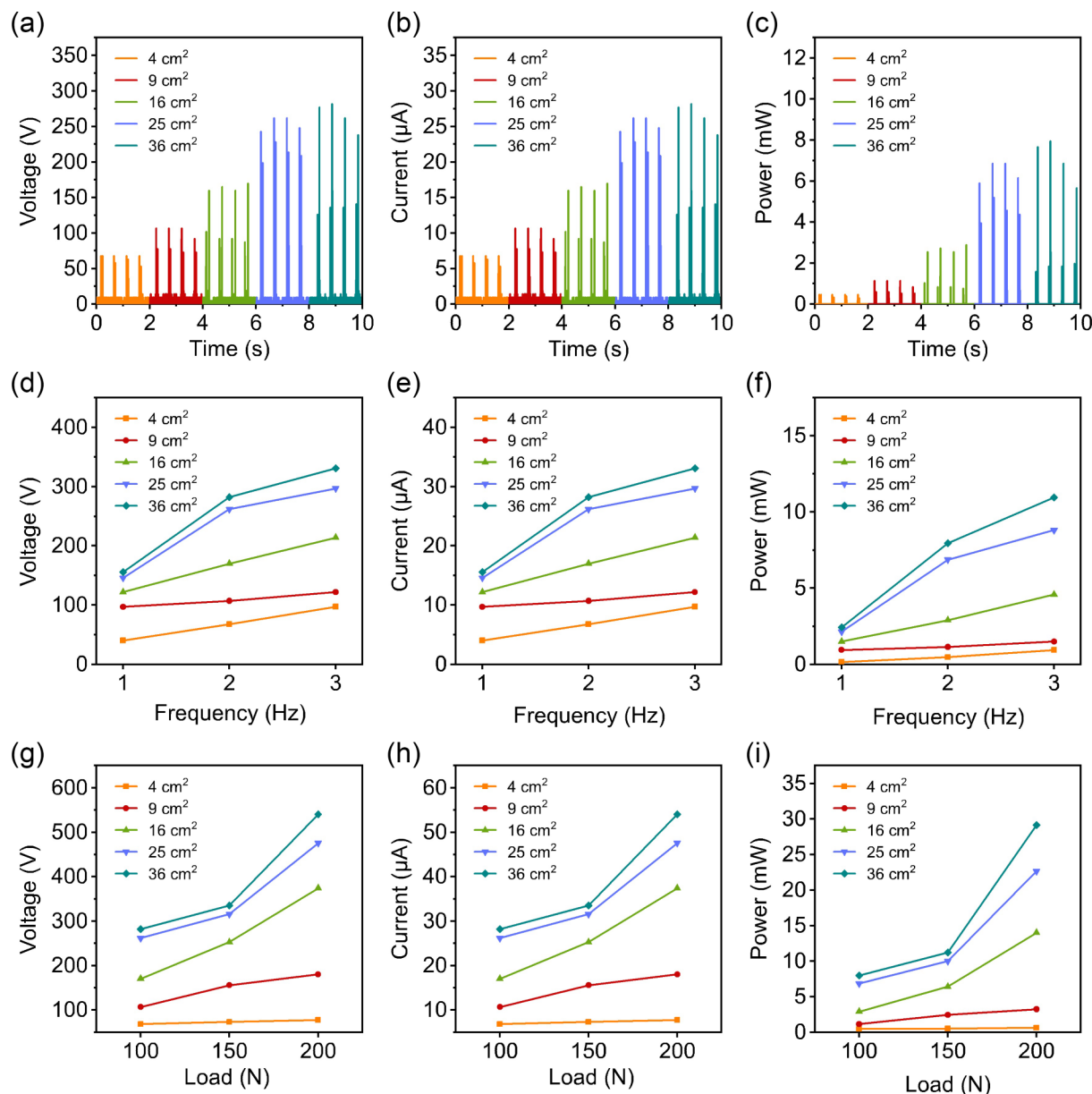
Figure 3 (a) Output voltages, (b) currents, and (c) electrical powers for different size TENGs. (d) Output voltages, (e) currents, and (f) electrical powers for various pulse frequencies. (g) Output voltages, (h) currents, and (i) electrical powers for various pulse forces.

1.49, 4.58, 8.82, and 10.96 mW for 3 Hz, respectively. The results show a linear relationship between the pulse frequency and the electrical parameters of TENGs. The voltage of a TENG increases with the impact frequency because more frequent contact-separation cycles generate charges at a higher rate and enhance charge density on the surfaces, leading to a greater potential difference. The shorter time intervals between impacts reduce charge recombination, retaining more charges and thus increasing the voltage. Additionally, the rapid mechanical motion at higher frequencies enhances the effectiveness of charge transfer and separation, while the cumulative effect of overlapping voltage pulses contributes to a higher average voltage output. These combined factors result in a higher voltage as the impact frequency rises.

Figures 3(g)−3(i) depict the relationships between force and electrical parameters of the TENGs. The pulse frequency is fixed at 2 Hz for all force levels. In Fig. 3(g), the TENG output voltages for applied forces of 100 N are 68, 107, 170, 262, and 282 V, respectively. For 150 N, the output voltages are 72.9, 156, 253, 316, and 335 V, respectively. For 200 N, the voltages are 77.8, 180, 374, 476, and 540 V, respectively. The magnitude of improvement in output voltage increases nonlinearly with the size of the TENGs. For example, the output voltages of the 4 cm^2 TENG under 100 N and 200 N force levels are 68 and 77.8 V, respectively, indicating a voltage recovery of 14.4%. However, for the 36 cm^2 TENG, the output voltages under 100 and 200 N force levels are 282 and 540 V, respectively, demonstrating a voltage recovery of 91.5%. This result can be attributed to the higher pressure per unit area experienced by small-sized TENGs, bringing them closer to the force saturation points.

Figure 3(h) shows the current values of TENGs. In general, it is observed that an increase in applied force proportionally improves the performance of TENG significantly as the effective surface area expands. The measured current values for forces of 100, 150, and 200 N at 4 cm^2 TENG are 6.80, 7.29, and 7.78 μA, respectively. Although the external force has doubled, the current increase is 14.4%. Similarly, the measured current values for forces of 100, 150, and 200 N for 36 cm^2 TENG are 28.20, 33.50, and 54.00 μA, respectively. While the applied force is doubled, the current produced is 92.9% higher. The limited increase in smaller-sized TENGs is due to the higher force per unit area and near force saturation point. Figure 3(i) shows the electrical power output of

TENGs at three distinct power levels. Peak powers for 200 N force are 0.61 mW (1.53 W/m^2), 3.24 mW (3.60 W/m^2), 13.99 mW (8.74 W/m^2), 22.66 mW (9.06 W/m^2), and 29.16 mW (8.10 W/m^2). The peak power output is harvested from 36 cm^2 TENGs, while 25 cm^2 TENGs exhibit the highest power density.

The output voltage of vertical contact mode TENGs is influenced by various parameters, including but not limited to the ambient temperature, humidity, amplitude of external force, dielectric material properties, and effective contact surface area. Assuming constant environmental conditions, the output voltage of the TENGs can be expressed as follows

$$V = -\frac{1}{C(x)} Q_{SC}(x) + V_{OC}(x) \qquad (11)$$

where Q_{SC} is transfer charge, C is effective capacitance, V_{OC} is open circuit voltage, and x is the distance between two dielectrics. The equation for the short circuit case ($V = 0$) can be arranged as follows

$$Q_{SC}(x) = C(x) V_{OC}(x) \qquad (12)$$

$C(x)$ plays a crucial role in determining the current output of TENGs. The effective capacitance can be calculated using the following equation

$$C = \frac{\varepsilon A}{d} \qquad (13)$$

where ε is the dielectric constant, A is the surface area, and d is the thickness of the dielectric. As can be seen from Eqs. (12) and (13), increasing the ε/d ratio and A are the two main ways to improve the output power of TENGs. However, increasing the A value improves the output power of TENGs within a limited range due to dielectric losses. Many factors affect dielectric losses, and the mathematical model of capacitors can be used to determine them. Figures S3(a) and S3(b) in the ESM show a dielectric material's parallel *RC* equivalent circuit and current phasor diagram. *R* indicates the ohmic resistance causing dielectric losses, and *C* indicates the charge storage capacity of the dielectric material.

The dielectric leakage current (I_R) and charge current (I_C) can be written using the phasor diagram.

$$I_R = I_C \cdot \tan\delta \qquad (14)$$

$$I_C = \frac{V}{X_C} = \omega \cdot C \cdot V \qquad (15)$$

In this case, the I_C obtained in Eq. (15) is substituted in Eq. (14);

$$I_R = \omega \cdot C \cdot V \cdot \tan\delta \qquad (16)$$

Equality is achieved. The dielectric losses (P_L) can be written as follows

$$P_L = V \cdot I_R \qquad (17)$$

$$P_L = V \cdot \omega \cdot C \cdot V \cdot \tan\delta \qquad (18)$$

Finally, by simplifying Eq. (18), the dielectric losses can be expressed as follows.

$$P_L = V^2 \cdot \omega \cdot C \cdot \tan\delta \qquad (19)$$

Due to the quadratic ratio, the dielectric losses in a material are primarily affected by the voltage (V) to which the material is exposed. The frequency of the applied voltage is also an essential factor as dielectric losses increase directly with the frequency since $\omega = 2\pi f$. Furthermore, increasing a material's capacitance (C) increases the stored charge and leads to higher dielectric losses.

Equations (12) and (13) demonstrate that the surface area of the TENG directly enhances its output voltage. However, Eq. (19) reveals that dielectric losses increase exponentially with the square of the output voltage. The increasing dielectric losses lead to a paradoxical situation where the TENG's output performance improves with an increase in the surface area up to an optimum value. Beyond this optimum value, further increases in the surface area do not result in a corresponding increase in output voltage due to dramatically rising dielectric losses. Hence, optimizing the surface area of the dielectric is crucial to enhancing the energy density of TENGs.

Figures S4(a) and S4(b) in the ESM illustrate the impact of dielectric surface area and thickness on the output power of TENGs. As shown in Fig. S4(a) in the ESM, increasing the surface area of the dielectric enhances its charge storage capacity. However, as indicated in Eq. (19), the exponential increase in dielectric losses due to the voltage output causes low dielectric efficiency. Therefore, each dielectric material has an optimum surface area that maximizes the power density output. Figure S4(b) in the ESM illustrates the impact of dielectric thickness on the output power of TENGs. Increasing the dielectric thickness leads to a decrease in the electrostatic effect, which reduces the amount of opposite polarization between the plates. However, it also increases the charge capacity. These relationships highlight the importance of optimizing the dielectric thickness to achieve maximum energy density in TENGs.

Load impedance is a crucial factor that affects the output power of TENGs. The output performance of TENGs can exhibit significant changes when a capacitive load is connected instead of the ohmic load used in previous experiments. Figure 4(a) illustrates the maximum voltage values and total transfer charge of TENGs of different sizes at 22 nF capacitive load at 2 Hz and 100 N pulses. The maximum voltages generated at the load are 238, 334, 669, 574, and 574 mV, respectively. Using Eq. (4), the total charge stored in the capacitor is 5.26, 7.36, 14.72, 12.63, and 12.63 nC, respectively. While the voltage increased as the size increased in ohmic load, the voltage decreased after 4 cm × 4 cm in capacitive load. This decrease is due to the increase in dielectric losses of TENGs and the decrease in energy storage per unit area. Figure 4(b) demonstrates the energy stored in TENGs and the energy density per unit area. The energy obtained was calculated as 0.63, 1.23, 4.92, 3.62, and 3.62 nJ, respectively, using Eq. (3). Energy densities were obtained as 0.16, 0.14, 0.31, 0.14, and 0.10 nJ/cm^2, respectively. Maximum values for both energy and energy density were obtained at 4 cm × 4 cm.

The dielectric properties of materials significantly influence the performance, efficiency, and reliability of TENGs. Figure 4(c) displays the dielectric constant (ε') and dielectric losses (ε'') of TENGs under 200 kHz and 2 V. As the size of TENGs increases, a noticeable trend emerges, dielectric constants tend to decrease while dielectric losses increase. Larger TENGs store more energy, increasing the output power. However, increasing TENG sizes cause an increase in dielectric losses and leakage currents, which ultimately reduces energy efficiency. This interaction causes the energy density to rise to a peak at the optimum size and decrease beyond that.

Figure 4(d) presents the capacitance per unit area (C_d) and C_m values of TENGs. C_m values of the TENGs were measured as 25.43, 50, 82.07, 102, and 135 pF. The corresponding C_d values were 6.36, 5.56, 5.13, 4.08, and 3.75 pF/cm^2, respectively. As the size of the TENGs increases, the C_m value also increases, while the C_d value decreases. The decrease in C_d resulted in a reduction of the energy density harvested from the TENGs. In addition to the size, equivalent DC resistance (R_{DC}) affects the output performance of TENGs. The *I*–*V* characteristic of TENGs was
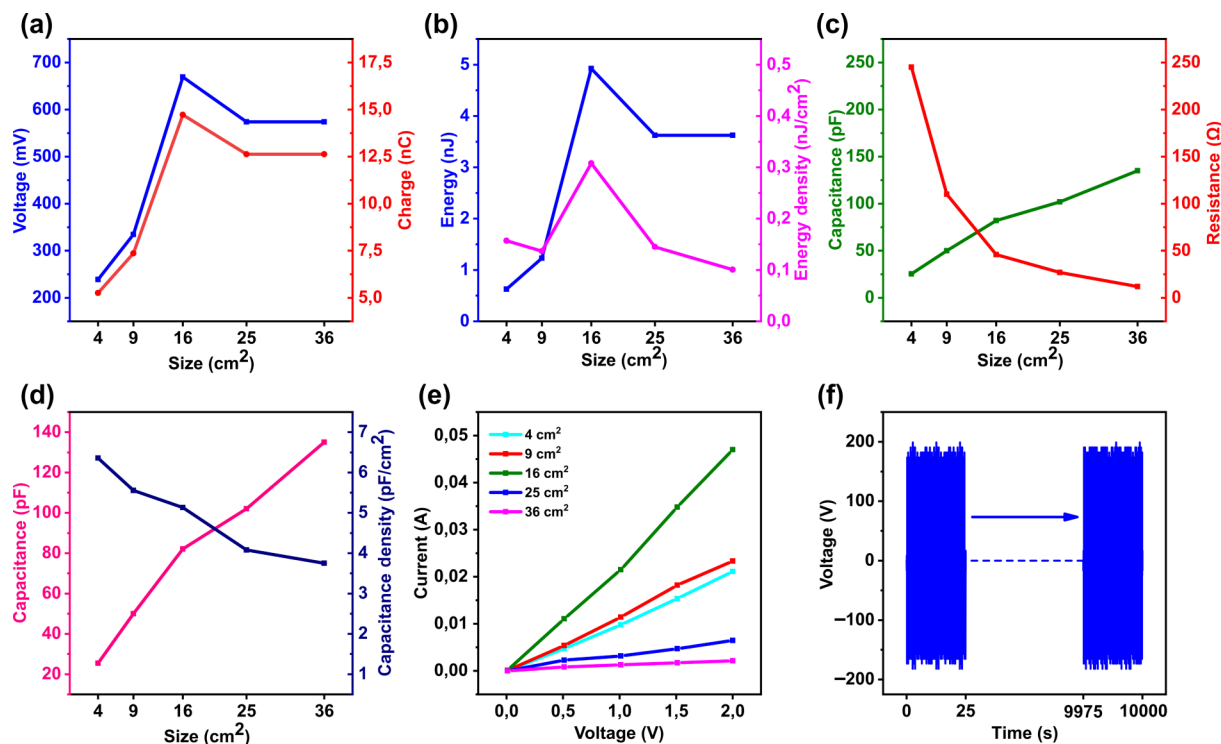
Figure 4 (a) Maximum voltage–charge curves, (b) energy and energy density curves, (c) capacitance and resistance curves, (d) capacitance and capacitance density curves, (e) *I–V* characteristics for the TENGs of different sizes, and (f) high frequency and low-force fatigue test results for 4 cm × 4 cm TENG.

analyzed, and as shown in Fig. 4(e), the highest and lowest current was produced by the 16 and 36 cm² TENGs, respectively. Using Ohm's law, it was determined that the 16 cm² TENG has the lowest R_{DC}. The results indicated that R_{DC} is an important factor affecting energy density, and TENGs with lower R_{DC} can achieve higher energy density.

Another advantage of TENGs made of white silicone and glass fiber in vertical contact mode is their longevity. As shown in Fig. 4(f), a fatigue test was conducted on a 4 cm × 4 cm TENG at 4 Hz frequency and 20 N force. Due to the low force used in fatigue testing, TENG's output voltage is lower than previous results. Despite the long test period, the TENG voltage amplitude has not decreased. These results demonstrate that TENGs made of glass fiber and silicone are suitable for long-life use, high-energy conversation efficient, and easy to manufacture.

3.3 Multi-cell TENGs

The optimization results of dielectric size obtained in this study indicate that TENGs with a surface area larger than the optimum value experience a decrease in energy density. Therefore, multicell layers with smaller dielectrics should be developed for large-scale TENGs with high energy density. Smaller cells can be integrated in parallel to produce large-scale multicell TENGs. Due to its complex, unstable, and non-linear voltage-generating characteristic, the equivalent output voltage obtained by connecting TENGs in parallel may differ from conventional electrical power sources. In voltage sources connected in parallel, the equivalent output voltage takes the average value of the sources and the current capacity increases in proportion to the number of sources. Horizontal and vertical multicell TENGs were fabricated to analyze the effect of parallel integration of cells on the output voltage. The energy conversion efficiency results of multicell structures with different configurations will guide the design of large-scale TENGs.

Figure 5(a) illustrates the output voltages of a 4 cm × 4 cm vertical multicell TENG with a capacitance of 0.022 μF, varying based on the number of cells. A fatigue machine applied a 20 N

force at a frequency of 4 Hz to the vertical multicell TENG. The maximum voltages generated by the 1, 2, 3, and 4-cell TENGs were approximately 10, 18, 27, and 36 V, respectively. The data show a linear relationship between the output voltage of the TENGs and the number of cells. Additionally, it is observed that the oscillation in the waveform increases as the generated voltage rises. This can be attributed to the increased discharge rate as the capacitance-voltage rises. Figure 5(b) presents the vertical multicell TENG output voltages under a 0.1 μF capacitive load. The maximum voltages generated by the 1, 2, 3, and 4-cell TENGs were approximately 8, 15, 22, and 28 V, respectively. Compared to the 0.022 μF load, the charge–discharge oscillation is reduced at the 0.1 μF load. It can be concluded that there is a proportional increase between the output voltage and the number of cells. Figure 5(c) displays the vertical multicell TENG output voltages under a 0.5 μF capacitive load. The maximum voltages generated by the 1, 2, 3, and 4-cell TENGs were approximately 7, 13, 19, and 25 V, respectively. The linear increase in output voltage, depending on the number of cells, continues at the 0.5 μF load. Lastly, Fig. 5(d) demonstrates the vertical multicell TENG output voltages under a 1 μF capacitive load. The maximum voltages generated by the 1, 2, 3, and 4-cell TENGs were approximately 7.5, 12.5, 17.5, and 20 V, respectively. As the number of cells increases, the rate of increase in output voltage reduces. The linear relationship observed between the output voltage and the number of cells at previous loads disrupts at the 1 μF load. This result is attributed to the non-linear relationship between the load impedance and the TENG output voltage.

Figure 5(e) illustrates the output voltages of a horizontal multicell TENG, composed of 4 cm × 4 cm cells, for a 0.022 μF capacitive load. A force of 20 N at a frequency of 4 Hz was applied to the horizontal multicell TENG using a fatigue machine. The horizontal multicell TENG consists of 4 series of 6 cells. The maximum voltages generated by the 6, 12, 18, and 24-cell TENGs were approximately 23, 28, 40, and 53 V, respectively. It is evident that the output voltage increases in a limited manner with the increase in the number of cells, and this increase is non-linear.
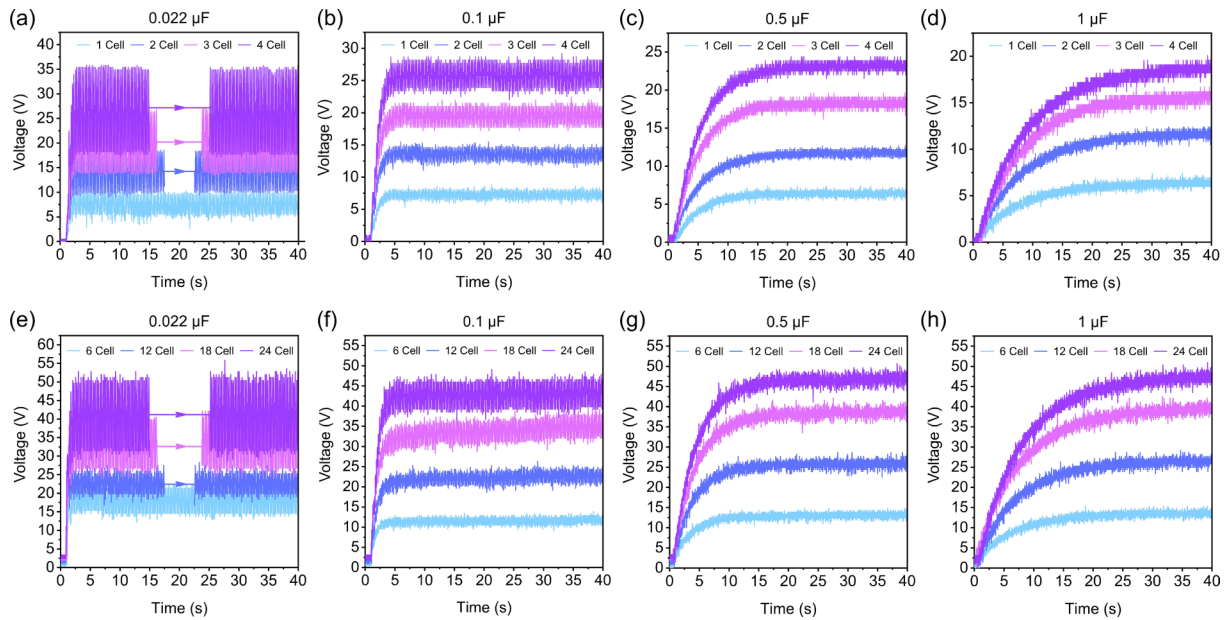
Figure 5 Output voltages and stored energy of vertical TENGs in different cell numbers under (a) 0.022, (b) 0.1, (c) 0.5, and (d) 1 μF capacitance. Output voltages of horizontal TENGs in different cell numbers under (e) 0.022, (f) 0.1, (g) 0.5, and (h) 1 μF capacitive load.

This behavior is caused by some cells producing low voltages due to the asynchronous distribution of the pulse force over the cells. Figure 5(f) presents the horizontal multicell TENG output voltages under a capacitance load of 0.1 μF. The maximum voltages produced by the 6, 12, 18, and 24-cell TENGs were approximately 13, 25, 40, and 49 V, respectively. The voltage increase in the first three series is approximately linear but with the addition of Series 4, the voltage increase becomes limited.

Figure 5(g) displays the horizontal multicell TENG output voltages under a 0.5 μF capacitive load. The maximum voltages produced by the 6, 12, 18, and 24-cell TENGs were approximately 14, 28, 42, and 51 V, respectively. Although the capacitance load increased to 0.5 μF compared to 0.1 μF, it is noticed that the maximum voltage generated did not change significantly, but the charging time increased to some extent. Lastly, Fig. 5(h) demonstrates the horizontal multicell TENG output voltages under a 1 μF capacitive load. The maximum voltages produced by the 6, 12, 18, and 24-cell TENGs were approximately 14, 29, 42, and 52 V, respectively. At a 1 μF capacitive load, it can be observed that the charging time is reduced compared to the previous loads, but the maximum output voltages remain similar.

The power generation performances of vertical and horizontal multicell TENGs can be compared through lighting applications. The results obtained from three different LED lighting applications are presented in Fig. S5 in the ESM. The first group consisted of 100 pieces of 5 mm Red LEDs, the second group comprised 10 LEDs rated at 3 V and 1 W, and the third group consisted of 30 strip LEDs rated at 12 V. The LEDs in all groups were connected in parallel. The LEDs in the first group exhibited capacitive impedance, while those in the other two groups exhibited ohmic impedance. The total impedances of the LED groups were measured as follows: $Z_1 = 184.03 - \text{j}272.07$ kΩ for the first group, $Z_2 = 72.1 - \text{j}0.1$ Ω for the second group, and $Z_3 = 64.4 - \text{j}0.0014$ kΩ for the third group. It is seen that the impedance amplitude of Z_2 is very low compared to Z_1 and Z_3.

The illumination levels obtained from the LED applications can be seen in Fig. S5 in the ESM. It can be observed that the amount of light increases with the number of cells in the vertical multicell TENGs. However, the amount of light obtained from TENGs with 3 and 4 cells is close to each other. Similarly, in the horizontal multicell TENGs, the illumination of the LED groups increases with the number of cells. Generally, the 4-cell vertical TENGs

exhibit better illumination performance than the 6-cell horizontal TENGs. There are two main reasons for this outcome. The first reason is the more synchronous operation of the vertical multicell TENGs, which results in a cumulative increase in the generated energy. On the other hand, the asynchronous operation of cells in the horizontal multicell TENGs leads to a decrease in the total energy generated. The second reason is the integration of vertical multicell TENGs after the bridge diode, whereas the cells in the horizontal multicell TENG subgroups are in direct contact. This finding indicates that the amount of harvested energy increases when TENGs are integrated over the bridge diode, as seen in the vertical multicell TENGs. These results demonstrate that the vertical multicell TENGs exhibit improved energy harvesting and illumination performance due to their synchronous operation and integration after the bridge diode.

The study comparing vertical and horizontal multicell TENGs with capacitive load and LED applications determined that the vertical integration of TENGs is more efficient. Another important finding from the LED applications is the impact of load impedance on energy efficiency. Specifically, the equivalent impedance of the second group's LEDs was significantly lower than the other groups. When examining the LED lighting results for the second group, it was observed that the increase in light intensity was limited compared to the increase in the number of cells. This limitation can be attributed to low impedance loads approach saturation, and an increase in the power supplied does not significantly increase output power. These findings highlight the importance of impedance matching between the power source and the load in large-scale TENG designs to achieve high energy efficiency.

Findings so far reveal that large-size TENGs with high power density should consist of small-size sub-cells, which should be integrated via bridge diodes. Multi-layered and synchronous motion TENG (Synch-TENG) was designed per these principles shown in Fig. S6 in the ESM. The lower and upper layers of Synch-TENG are bonded to each other separately. The lower layers are stationary during operation, while the upper layers move synchronously. The most crucial advantage of synchronous motion is that the moving distance is only that of one layer, regardless of the number of multi-layers. In this way, multiple TENGs can operate simultaneously with short-distance movements. However, the external force applied in Synch-TENG

is shared equally between the layers. Synch-TENGs are more suitable for high-pressure applications such as step motion, as the performance of TENGs will be adversely affected by force distribution. Figure S6 in the ESM shows a large-size TENG designed for human step motion. The large-sized TENG consists of 16 Synch-TENGs and 64 cell groups. 40 cm × 40 cm laminated plywood was used on the lower and upper shields to distribute the applied force evenly on the Synch-TENGs. To observe the amount of energy produced, 160 LEDs of 12 V were connected to the large-size TENG as a load. As seen in Fig. S6 in the ESM, 160 LEDs glow brightly in the dark with step movement. Considering the short motion distance and the amount of power obtained, it is seen that the large-sized TENG working with step motion can be used in various electricity generation scenarios in daily life.

4 Conclusions

This study aimed to investigate the optimum dielectric sizes and layout configurations for large-scale TENGs with high energy density. The significant findings are summarized below.

- To achieve maximum energy density, the optimum dielectric thickness must be determined, which balances the electrostatic force and the transfer charge capacity.

- Dielectrics with surface areas larger than the optimum surface area reduce the energy density even though they increase the total power due to increased dielectric losses.

- In the design of multicell TENGs, vertical integration is more efficient than horizontal integration because it is more compatible with synchronous operation.

- Integrating multi cells via bridge diode instead of directly integrating them increases energy efficiency.

- Load impedance significantly affects the power generation characteristics of single and multicell TENGs.

The obtained findings determine the basic principles that should be considered in the design of large-scale TENGs. Considering the potential application areas, large-scale TENGs can play a significant role in converting waste energy into usable energy.

Acknowledgements

Electronic Supplementary Material: Supplementary material (circuit connection diagram of multi-cell TENGs, equivalent circuit model, equivalent circuit and current phasor diagram of a dielectric material, optimization curves depending on dielectric surface area and dielectric thickness, illumination levels of various LEDs depending on the number of TENG cells, and LED lighting applications of the large-scale TENG consists of 16 Synch-TENGs) is available in the online version of this article at https://doi.org/10.1007/s12274-024-6821-0.

References

[1] Dong, L.; Wang, M. X.; Wu, J. J.; Zhu, C. H.; Shi, J.; Morikawa, H. Stretchable, adhesive, self-healable, and conductive hydrogel-based deformable triboelectric nanogenerator for energy harvesting and human motion sensing. *ACS Appl. Mater. Interfaces* **2022**, *14*, 9126–9137.

[2] Feng, Z. P.; He, Q.; Wang, X.; Liu, J.; Qiu, J.; Wu, Y. F.; Yang, J. Multimode human-machine interface using a single-channel and patterned triboelectric sensor. *Nano Res.* **2022**, *15*, 9352–9358.

[3] Xi, Y. H.; Hua, J.; Shi, Y. J. Noncontact triboelectric nanogenerator for human motion monitoring and energy harvesting. *Nano Energy* **2020**, *69*, 104390.

[4] Kuntharin, S.; Harnchana, V.; Klamchuen, A.; Sinthiptharakoon, K.; Thongbai, P.; Amornkitbamrung, V.; Chindaprasirt, P. Boosting the power output of a cement-based triboelectric nanogenerator by enhancing dielectric polarization with highly dispersed carbon black nanoparticles toward large-scale energy harvesting from human footsteps. *ACS Sustainable Chem. Eng.* **2022**, *10*, 4588–4598.

[5] Hossain, G.; Rahman, M.; Hossain, I. Z.; Khan, A. Wearable socks with single electrode triboelectric textile sensors for monitoring footsteps. *Sensor Actuat. A Phys.* **2022**, *333*, 113316.

[6] Hu, X. Y.; Feng, J. R.; Liang, C. J.; Ning, H.; Chen, C. J.; Li, J. Y.; Wen, H. G.; Yao, H. L.; Wan, L. Y.; Liu, G. L. Round-trip oscillation triboelectric nanogenerator with high output response and low wear to harvest random wind energy. *Nano Res.* **2023**, *16*, 11259–11268.

[7] Li, J. Q.; Chen, J.; Guo, H. Y. Triboelectric nanogenerators for harvesting wind energy: Recent advances and future perspectives. *Energies* **2021**, *14*, 6949.

[8] Zhang, C. G.; Liu, Y. B.; Zhang, B. F.; Yang, O.; Yuan, W.; He, L. X.; Wei, X. L.; Wang, J.; Wang, Z. L. Harvesting wind energy by a triboelectric nanogenerator for an intelligent high-speed train system. *ACS Energy Lett.* **2021**, *6*, 1490–1499.

[9] Zhang, C. G.; He, L. X.; Zhou, L. L.; Yang, O.; Yuan, W.; Wei, X. L.; Liu, Y. B.; Lu, L.; Wang, J.; Wang, Z. L. Active resonance triboelectric nanogenerator for harvesting omnidirectional water-wave energy. *Joule* **2021**, *5*, 1613–1623.

[10] Liang, X.; Jiang, T.; Liu, G. X.; Feng, Y. W.; Zhang, C.; Wang, Z. L. Spherical triboelectric nanogenerator integrated with power management module for harvesting multidirectional water wave energy. *Energy Environ. Sci.* **2020**, *13*, 277–285.

[11] Lou, Y.; Li, M. F.; Hu, J. X.; Zhao, Y. L.; Cui, W. Q.; Wang, Y. L.; Yu, A. F.; Zhai, J. Y. Maximizing the energy conversion of triboelectric nanogenerator through the synergistic effect of high coupling and dual-track circuit for marine monitoring. *Nano Energy* **2024**, *121*, 109240.

[12] Zhu, Q. Q.; Liao, W. Q.; Sun, C.; Qin, X.; Zhang, F. J.; Ji, H. F.; Li, Y. Q.; Wen, Z.; Sun, X. H. Highly stretchable, conductive, and wide-operating temperature ionogel based wearable triboelectric nanogenerator. *Nano Res.* **2023**, *16*, 11638–11645.

[13] Yang, Y. Q.; Guo, X. G.; Zhu, M. L.; Sun, Z. D.; Zhang, Z. X.; He, T. Y. Y.; Lee, C. Triboelectric nanogenerator enabled wearable sensors and electronics for sustainable internet of things integrated green earth. *Adv. Energy Mater.* **2023**, *13*, 2203040.

[14] Sardo, F. R.; Rayegani, A.; Nazar, A. M.; Balaghiinaloo, M.; Saberian, M.; Mohsan, S. A. H.; Alsharif, M. H.; Cho, H. S. Recent progress of triboelectric nanogenerators for biomedical sensors: From design to application. *Biosensors (Basel)* **2022**, *12*, 697.

[15] Feng, X.; Zhang, Y.; Kang, L.; Wang, L. C.; Duan, C. X.; Yin, K.;

Pang, J. B.; Wang, K. Integrated energy storage system based on triboelectric nanogenerator in electronic devices. *Front. Chem. Sci. Eng.* **2021**, *15*, 238–250.

[16] Dong, K.; Wang, Z. L. Self-charging power textiles integrating energy harvesting triboelectric nanogenerators with energy storage batteries/supercapacitors. *J. Semicond.* **2021**, *42*, 101601.

[17] Zhao, Z. H.; Zhou, L. L.; Li, S. X.; Liu, D.; Li, Y. H.; Gao, Y. K.; Liu, Y. B.; Dai, Y. J.; Wang, J.; Wang, Z. L. Selection rules of triboelectric materials for direct-current triboelectric nanogenerator. *Nat. Commun.* **2021**, *12*, 4686.

[18] Si, J. H.; Duan, R. G.; Zhang, M. L.; Liu, X. M. Recent progress regarding materials and structures of triboelectric nanogenerators for AR and VR. *Nanomaterials (Basel)* **2022**, *12*, 1385.

[19] Zhang, R. Y.; Olin, H. Material choices for triboelectric nanogenerators: A critical review. *EcoMat* **2020**, *2*, e12062.

[20] Topçu, M. A.; Karabiber, A.; Sarılmaz, A.; Koç, F.; Özel, F. Performance-enhanced of triboelectric nanogenerator based on functionalized silicone with pumice for energy harvesting. *Sustain. Energy Technol. Assess.* **2023**, *57*, 103251.

[21] Arkan, E.; Karabiber, A.; Topçu, M. A.; Kinas, Z.; Sarilmaz, A.; Ozel, S. S.; Ozel, F. Nano-ceria based TENGs: Effect of dopant structure on energy harvesting performance. *Surf. Interfaces* **2023**, *37*, 102683.

[22] Ozen, A.; Karabiber, A.; Kınas, Z.; Ozel, F. High-power triboelectric nanogenerator based on enriched polyvinylpyrrolidone nanofibers for energy harvesting. *Phys. Status Solidi A* **2022**, *219*, 2100665.

[23] Arkan, M. Z. Y.; Kınas, Z.; Arkan, E.; Gökçe, C. O.; Kara, K.; Karabiber, A.; Kuş, M.; Özel, F. Molecular engineering-device efficiency relation: Performance boosting of triboelectric nanogenerator through doping of small molecules. *Int. J. Energy Res.* **2022**, *46*, 23517–23529.

[24] Gao, Y. Y.; Li, Z. H.; Xu, B. G.; Li, M. Q.; Jiang, C. H. Z.; Guan, X. Y.; Yang, Y. J. Scalable core-spun coating yarn-based triboelectric nanogenerators with hierarchical structure for wearable energy harvesting and sensing via continuous manufacturing. *Nano Energy* **2022**, *91*, 106672.

[25] Li, Y. H.; Guo, Z. T.; Zhao, Z. H.; Gao, Y. K.; Yang, P. Y.; Qiao, W. Y.; Zhou, L. L.; Wang, J.; Wang, Z. L. Multi-layered triboelectric nanogenerator incorporated with self-charge excitation for efficient water wave energy harvesting. *Appl. Energy* **2023**, *336*, 120792.

[26] Tao, K.; Chen, Z. S.; Yi, H. P.; Zhang, R. R.; Shen, Q.; Wu, J.; Tang, L. H.; Fan, K. Q.; Fu, Y. Q.; Miao, J. M. et al. Hierarchical honeycomb-structured electret/triboelectric nanogenerator for biomechanical and morphing wing energy harvesting. *Nano-Micro Lett.* **2021**, *13*, 123.

[27] Shen, F.; Zhang, D.; Zhang, Q.; Li, Z. J.; Guo, H. Y.; Gong, Y.; Peng, Y. Influence of temperature difference on performance of solid-liquid triboelectric nanogenerators. *Nano Energy* **2022**, *99*, 107431.

[28] Wen, R. M.; Guo, J. M.; Yu, A. F.; Zhai, J. Y.; Wang, Z. L. Humidity-resistive triboelectric nanogenerator fabricated using metal organic framework composite. *Adv. Funct. Mater.* **2019**, *29*, 1807655.

[29] Lu, S.; Lei, W. Q.; Gao, L. X.; Chen, X.; Tong, D. Q.; Yuan, P. F.; Mu, X. J.; Yu, H. Regulating the high-voltage and high-impedance characteristics of triboelectric nanogenerator toward practical self-powered sensors. *Nano Energy* **2021**, *87*, 106137.

[30] Kim, S. W.; Kim, J. K.; Kim, H. J.; Cao, C. T.; Oh, N. K.; Yang, Y.; Song, H. C.; Shim, M.; Park, H. S.; Baik, J. M. Output signals control of triboelectric nanogenerator with metal-dielectric-metal configuration through high resistance grounded systems. *Nano Energy* **2022**, *95*, 107023.

[31] Wang, Z. X.; Wu, Y. H.; Jiang, W. B.; Liu, Q. Y.; Wang, X. B.; Zhang, J. W.; Zhou, Z. Y.; Zheng, H. W.; Wang, Z. F.; Wang, Z. L. A universal power management strategy based on novel sound-driven triboelectric nanogenerator and its fully self-powered wireless system applications. *Adv. Funct. Mater.* **2021**, *31*, 2103081.

[32] Liu, D.; Zhou, L. L.; Cui, S. N.; Gao, Y. K.; Li, S. X.; Zhao, Z. H.; Yi, Z. Y.; Zou, H. Y.; Fan, Y. J.; Wang, J. et al. Standardized measurement of dielectric materials' intrinsic triboelectric charge density through the suppression of air breakdown. *Nat. Commun.* **2022**, *13*, 6019.

[33] Zhang, Z.; Sun, X. F.; Chen, Y.; Debeli, D. K.; Guo, J. Comprehensive dependence of triboelectric nanogenerator on dielectric thickness and external impact for high electric outputs. *J. Appl. Phys.* **2018**, *124*, 045106.

[34] Okbaz, A.; Karabiber, A.; Yar, A.; Kınas, Z.; Sarılmaz, A.; Ozel, F. High-performance triboelectric nanogenerator with optimized Al or Ti-embedded silicone tribomaterial. *Energy Convers Manag.* **2022**, *252*, 115053.

[35] Zou, Y. J.; Xu, J.; Chen, K.; Chen, J. Advances in nanostructures for high-performance triboelectric nanogenerators. *Adv. Mater. Technol.* **2021**, *6*, 2000916.

[36] Li, Z. K.; Liu, J. T.; Chi, M. S.; Miao, X.; Yang, H. X.; Cui, W. Q.; Yu, A. F.; Zhai, J. Y. Ultra-high output triboelectric nanogenerator based on synergies of material modification and charge pumping. *Chem. Eng. J.* **2024**, *481*, 148726.

[37] Dai, K. R.; Wang, X. F.; Niu, S. M.; Yi, F.; Yin, Y. J.; Chen, L.; Zhang, Y.; You, Z. Simulation and structure optimization of triboelectric nanogenerators considering the effects of parasitic capacitance. *Nano Res.* **2017**, *10*, 157–171.

[38] Yin, P. L.; Tang, L. H.; Li, Z. J.; Guo, H. Y.; Aw, K. C. Circuit representation, experiment and analysis of parallel-cell triboelectric nanogenerator. *Energy Convers. Manag.* **2023**, *278*, 116741.

[39] El-Mohandes, A. M.; Zheng, R. Active matching circuit to enhance the generated power of triboelectric nanogenerators. *Nano Energy* **2021**, *80*, 105588.

[40] Wang, H.; Fan, Z. Q.; Zhao, T. C.; Dong, J. L.; Wang, S. Y.; Wang, Y.; Xiao, X.; Liu, C. X.; Pan, X. X.; Zhao, Y. P. et al. Sandwich-like triboelectric nanogenerators integrated self-powered buoy for navigation safety. *Nano Energy* **2021**, *84*, 105920.

[41] Zhou, T.; Zhang, L. M.; Xue, F.; Tang, W.; Zhang, C.; Wang, Z. L. Multilayered electret films based triboelectric nanogenerator. *Nano Res.* **2016**, *9*, 1442–1451.

[42] Li, S. M.; Wang, J.; Peng, W. B.; Lin, L.; Zi, Y. L.; Wang, S. H.; Zhang, G.; Wang, Z. L. Sustainable energy source for wearable electronics based on multilayer elastomeric triboelectric nanogenerators. *Adv. Energy Mater.* **2017**, *7*, 1602832.

[43] Xiao, T. X.; Liang, X.; Jiang, T.; Xu, L.; Shao, J. J.; Nie, J. H.; Bai, Y.; Zhong, W.; Wang, Z. L. Spherical triboelectric nanogenerators based on spring-assisted multilayered structure for efficient water wave energy harvesting. *Adv. Funct. Mater.* **2018**, *28*, 1802634.

[44] Bai, P.; Zhu, G.; Lin, Z. H.; Jing, Q. S.; Chen, J.; Zhang, G.; Ma, J. S.; Wang, Z. L. Integrated multilayered triboelectric nanogenerator for harvesting biomechanical energy from human motions. *ACS Nano* **2013**, *7*, 3713–3719.

[45] Topçu, M. A.; Karabiber, A.; Koç, F.; Sarılmaz, A.; Özel, F. Boron minerals with different crystal structures as performance manipulators in triboelectric nanogenerators. *Energy Technol.* **2024**, *12*, 2301282.

[46] Zhao, D.; Yu, X.; Wang, Z. J.; Wang, J. L.; Li, X.; Wang, Z. L.; Cheng, T. H. Universal equivalent circuit model and verification of current source for triboelectric nanogenerator. *Nano Energy* **2021**, *89*, 106335.

[47] Wang, J.; Zhang, B. F.; Zhao, Z. H.; Gao, Y. K.; Liu, D.; Liu, X. R.; Yang, P. Y.; Guo, Z. T.; Wang, Z. L.; Wang, J. Boosting the charge density of triboelectric nanogenerator by suppressing air breakdown and dielectric charge leakage. *Adv. Energy Mater.* **2024**, *14*, 2303874.